

Optical Pumping: Characterizing the Hyperfine Structures, Zeeman Interactions and Nuclear Spins of ^{85}Rb and ^{87}Rb

Ian Haines*

*Department of Physics, University of California,
Berkeley, 366 Physics North, Berkeley, CA 94720*

(Dated: October 19, 2021)

The Compton effect has its history in overturning the classical understanding of light scattering via free electrons. Compton's work proved to be important for the formulation and experimental validation of quantum mechanics. The Compton effect was observed for a ^{241}Am source and ^{13}Al targets with varying radii for 5 angles with a pulse-height analyzer. Results showed $\chi^2 = 0.0109$ for the Compton scattering hypothesis. The Compton Hypothesis was accepted. This acceptance showed the mass of the electron to be $m_e = 520 \pm 21$ keV. The Klein-Nishina hypothesis predicted the correct order of magnitude for electron scattering energies. Analysis and discussion of results is included.

Keywords: Optical pumping, Breit-Rabi, hyperfine, zeeman, spectroscopy, nuclear physics, atomic physics

I. INTRODUCTION

Spectroscopy, the branch of physics concerning the interactions between matter and light, has been a topic of interest for physicists for centuries going back to Isaac Newton's studies of sunlight dispersing within a glass prism [1]. Quantum mechanics provides a systematic way to study these interactions at small scales that classical physics cannot provide. One of the earlier insights furnished by quantum mechanics was the notion that atomic transitions from one bound state to another happen only when a fixed, specific amount of energy is either absorbed by or emitted from an atom so that all transitions between bound states compose a discrete spectrum [2]. The structure of atoms and their interactions can be understood then by a complete understanding of the transitions between bound states.

One way of forcing these atomic transitions is through a method called optical pumping. Specifically, the structure of alkali atoms, in particular ^{85}Rb and ^{87}Rb , can be elucidated via optical pumping [3]. Optical pumping works by subjecting a gas of Rb atoms to a magnetic field to create a preferred direction of quantization and then an electromagnetic radiation field to "pump" the gas away from an equilibrium distribution towards a nonequilibrium one which becomes transparent to the radiation eventually. These atoms are termed "optically dark" to the radiation field. By applying a radiofrequency (rf) field, the atoms can be broken out of their degenerate states back to a new equilibrium distribution which is opaque to the light again. This technique is called Optically Detected Magnetic Resonance or ODMR since the rf frequency is a resonant frequency of the Zeeman transitions. This technique is used to determine the nuclear spin of the atom since the rf field interaction depends upon the value of this quantity. Additionally, this tech-

nique is also used to verify the calculated resonant Zeeman transitions and the Breit-Rabi formula.

The magnetic field interactions with the atoms are treated through perturbation theory. The application of perturbation theory is best understood in the context of the vector model of angular momenta. The radiation field interaction is treated by finding which matrix elements of the dipole operator are non-zero. These non-zero elements say which transitions from $|a\rangle \rightarrow |b\rangle$ are allowed.

A. Vector Model of Angular Momenta

In ^{85}Rb and ^{87}Rb , henceforth Rb will refer to both isotopes unless otherwise specified, there are 36 electrons bound to the nucleus due to the Coulomb interaction and one valence electron in the $5s$ orbital. This electron can be specified by its spin angular momentum and orbital angular momentum, \mathbf{S} and \mathbf{L} , respectively, where $S = \frac{1}{2}$ and $L = 0, 1, 2, \dots$. The total electronic angular momentum is given by their sum $\mathbf{J} = \mathbf{L} + \mathbf{S}$. The rules of the addition of angular momenta yield $J = \frac{1}{2}, \frac{3}{2}, \frac{5}{2}, \dots$. In addition to this, the nucleus of Rb also has a spin angular momentum denoted \mathbf{I} ; and, $I = \frac{5}{2}$ for ^{85}Rb and $I = \frac{3}{2}$ for ^{87}Rb . The total angular momentum of Rb is therefore given by the sum $\mathbf{F} = \mathbf{I} + \mathbf{J}$. The rules of the addition of angular momenta yield $F = 1, 2, \dots$ [2].

B. Sketching the Perturbation Scheme

1. Energy Splitting from the Intrinsic Interaction

The hyperfine interaction occurs due to the interaction between the \mathbf{B} -field generated by the electronic angular momentum, and the nuclear magnetic moment,

$$\boldsymbol{\mu}_I = -g_I \mu_N \frac{\mathbf{I}}{\hbar},$$

* ianphaines@berkeley.edu

where g_I is the effective g-factor of the nucleus and μ_N is the nuclear magneton. The Hamiltonian has the form

$$\hat{\mathcal{H}}_{\text{hfs}} = -\boldsymbol{\mu}_I \cdot \mathbf{B}_J \propto \mathbf{J} \cdot \mathbf{I} \quad (1)$$

which splits the energy eigenvalues arising from the fine structure interaction (see Fig's 1 and 2). This splitting is due to the $(2S+1) \times (2L+1) \times (2I+1)$ combinations between the total electronic orbital angular momenta and nuclear spin eigenstates.

Using the fact that $\mathbf{F} = \mathbf{J} + \mathbf{I}$, 1 can be rewritten as

$$\hat{\mathcal{H}}_{\text{hfs}} \propto \frac{1}{2}(F^2 - J^2 - I^2) \quad (2)$$

implying that the desired basis to evaluate this term is the coupled basis. The eigenbasis vectors are given by $|I, J; F, m_F\rangle$ where $m_F = -F, -F+1, \dots, F-1, F$. These states can be obtained using the Clebsch-Gordan coefficients and the uncoupled basis vectors $|I, m_I; J, m_J\rangle$.

2. Zeeman Splitting in the Hyperfine Perturbation

In the presence of an external magnetic field whose wave vector is oriented parallel to the axis of quantization, the nuclear magnetic moment and electronic magnetic moment have a tendency to precess about the direction of motion of the field. As a result, the hyperfine structure Hamiltonian becomes

$$\hat{\mathcal{H}}_{\text{hfs+B}} = -\boldsymbol{\mu}_I \cdot (\mathbf{B}_J + \mathbf{B}_{\text{ext}}) - \boldsymbol{\mu}_J \cdot \mathbf{B}_{\text{ext}} \quad (3)$$

where \mathbf{B}_{ext} is the external magnetic field and

$$\boldsymbol{\mu}_J = g_J \mu_B \frac{\mathbf{J}}{\hbar}$$

is the magnetic moment of the electronic angular momentum where g_J is the Landé g-factor. The equation 3 can be rewritten as

$$\hat{\mathcal{H}}_{\text{hfs+B}} = \hat{\mathcal{H}}_{\text{hfs}} + \hat{\mathcal{H}}_B \quad (4)$$

where $\hat{\mathcal{H}}_B = -(\boldsymbol{\mu}_I + \boldsymbol{\mu}_J) \cdot \mathbf{B}_{\text{ext}}$. In the limit where \mathbf{B}_{ext} goes to zero, 1 is recovered.

C. The Weak Field Breit-Rabi Formula

In the case of optical pumping, the field is weak enough so that the hyperfine energies dominate the external field term [4]. Thus, the field term can be treated as a perturbation. The hyperfine Landé g-factor is given by

$$\begin{aligned} g_F &= g_I \frac{F(F+1) + I(I+1) - J(J+1)}{2F(F+1)} + \\ &g_J \frac{F(F+1) - I(I+1) + J(J+1)}{2F(F+1)} \\ &\approx g_J \frac{F(F+1) - I(I+1) + J(J+1)}{2F(F+1)} \end{aligned} \quad (5)$$

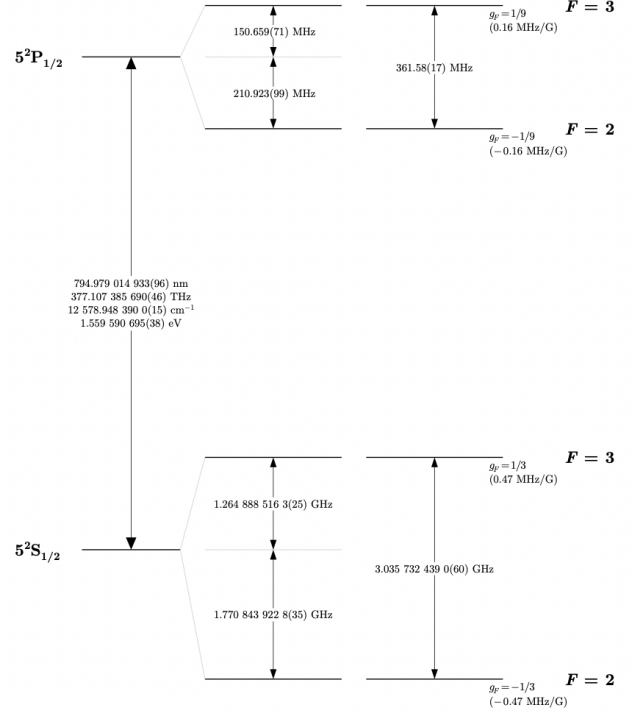


FIG. 1: ^{85}Rb D1 transitions for the hyperfine structure. Spacings for the hyperfine structure are scaled for those energies only and shouldn't be compared to the optical spacing. Figure taken from [4]

since $g_I \ll g_J$. Consequently, the second term in 4 can be rewritten as

$$\hat{\mathcal{H}}_B = g_F \mu_B \frac{\hat{F}_z}{\hbar} B_z. \quad (6)$$

In this case, the coupled basis is still a good basis to use to calculate the energy eigenvalues.

Applying 6 then yields the low-field Breit-Rabi formula

$$E_{F,m_F} = g_F \mu_B m_F B_z \quad (7)$$

In the electronic ground state, $F = I + \frac{1}{2}$, so

$$E_{F,m_F} = \frac{m_F \mu_B g_J}{2I+1} B_z$$

Hence, the energy differences for which $\Delta m_F = \pm 1$ are given by

$$h\nu = \frac{\mu_B g_J}{2I+1} B_z \quad (8)$$

where ν is the frequency of the rf field.

D. Optical Pumping and Selection Rules

The radiation field is characterized by a polarization vector $\hat{\epsilon} = \epsilon^+ \hat{\sigma}^+ + \epsilon^- \hat{\sigma}^-$ where the polarization basis

using the Helmholtz coil field strength. Thus, the resonant frequency of the Zeeman transitions and hence rf field can be found for any value of B_{HH} .

By applying a sinusoidal current to the rf generator and sweeping through a range of frequencies which covers the resonant frequencies for both ^{85}Rb and ^{87}Rb given a certain B_{HH} , ODMR can be observed (see Fig. 4).

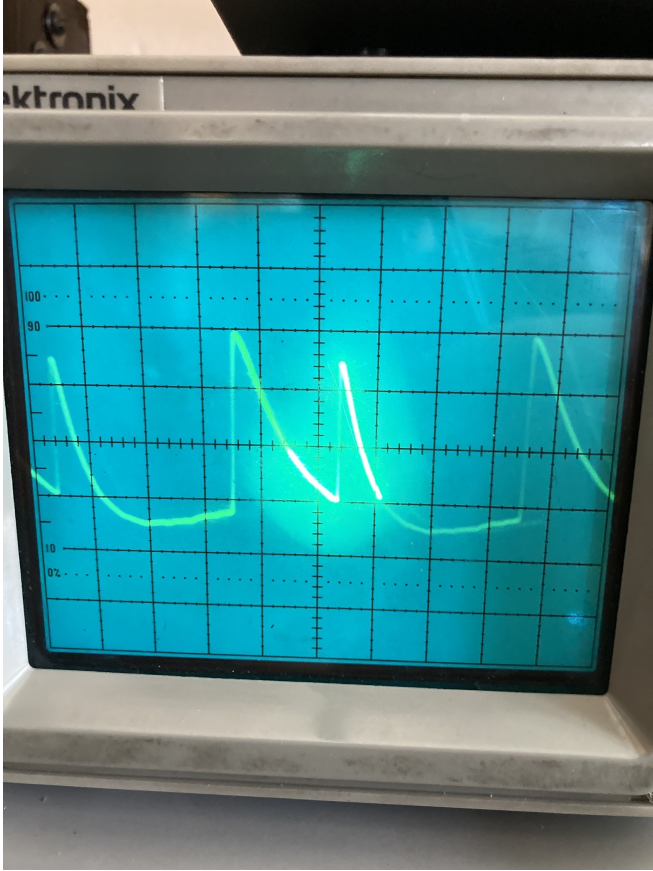


FIG. 4: Oscilloscope display of ODMR: the first observed sharp spike in the middle of the screen occurs when the $\nu_{\text{rf}} = \nu_{\text{Zeeman}}$ for ^{85}Rb since it has $I = 5/2$ while the second spike occurs when $\nu_{\text{rf}} = \nu_{\text{Zeeman}}$ for ^{87}Rb since it has $I = 3/2$

Another method to observe the ODMR is to fix the frequency of the rf field and change the strength of the Helmholtz coil field. This method is known as lock-in detection since it is used to extract the signal in spite of the noise within the environment. By carefully adjusting the Helmholtz coil field and switching the settings on the oscilloscope so that it displays a polar representation of the signal, Fig. 5 can be observed.

In addition to viewing ODMR, the timescales for optical pumping can be observed. The rf generator can be configured to generate a sinusoidal wave whose amplitude is modulated by a square wave. By configuring the oscilloscope to trigger at the proper times, Rabi oscillations can be observed as the spins re-orient themselves (see Fig. 6).

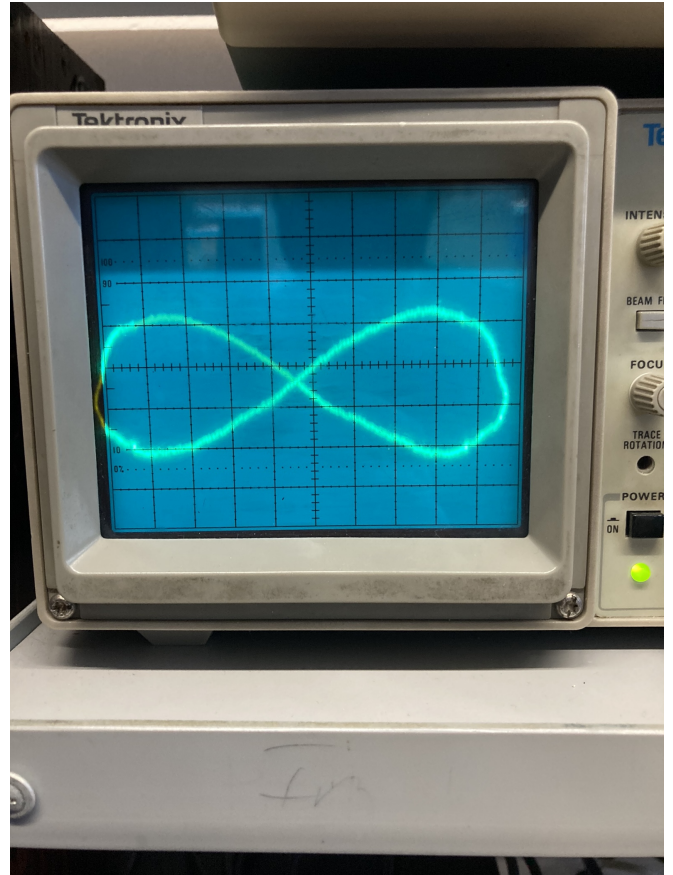


FIG. 5: Oscilloscope display of ODMR using the lock-in detection method. A strong resonant signal will display an evenly symmetric lemniscate that is not pinched on the sides.

2. Subtleties Involved

Important to note is that the field within the atomic vapor cell will not be exactly equal to the field due to the coil. Earth's ambient magnetic field is on the order of 0.25 to 0.65 gauss [6]. For a coil with $N = 135$, $I = 1\text{A}$, and $R = 27.5\text{cm}$, $B \approx 4.4$ gauss.

Another important aspect to note is that the heater used to excite the Rb atoms into a gas generates a magnetic field. The thermal radiation field is generated via resistive heating in a coil. Due to a changing electric field within the coil, Faraday's law states that a time-varying magnetic field is generated. Unlike Earth's ambient field, this field can be removed by turning the radiation field generator off while observing ODMR. The current dissipates within the coil on a timescale much faster than the ambient field generated by the coil within the vapor cell decreases and so ODMR can still be viewed for some time after the coil is turned off.

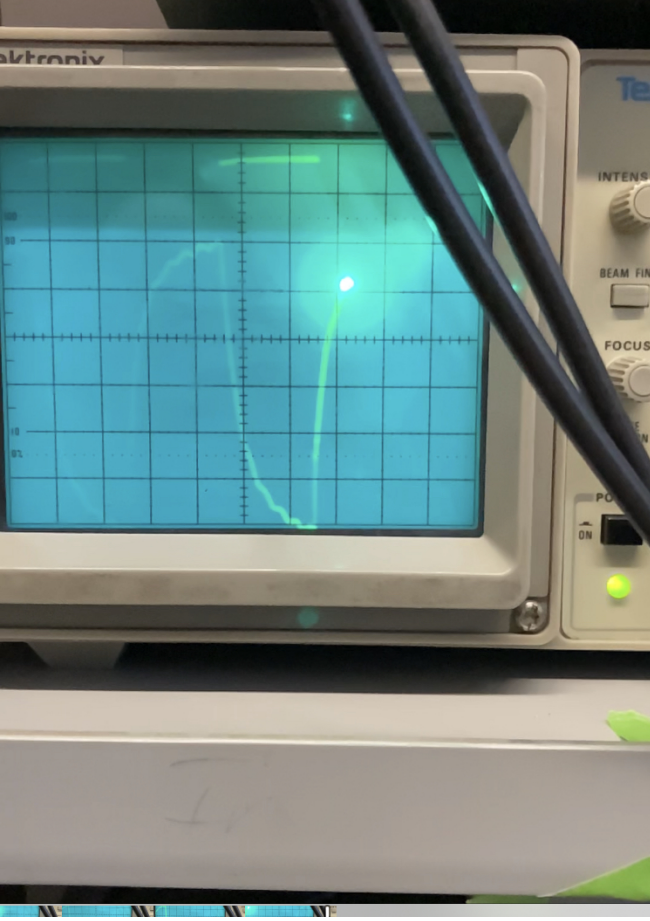


FIG. 6: Oscilloscope display of Rabi oscillations and spin re-alignment. The time it takes to pump can be measured by how long it takes for the signal to decay back down to zero.

C. Results and Analysis

The resonant frequencies were calculated for currents on the interval $[-3.0 \text{ A}, 3.0 \text{ A}]$ in steps of 0.5 A . From these frequencies, the currents were varied until the clearest resonance picture displayed on the oscilloscope (see Fig. 5). The frequencies as well as the nominal and real current values can be found in Table 1.

The data followed a linear relationship for both isotopes. A weighted least squares had been performed on four different sets of data: the negative current data for both isotopes and the positive current data for both isotopes (See Fig's 7-10). The slopes for positive and negative polarities for one isotope differed by roughly a percent. A weighted linear regression could be run just once for each isotope by combining the two polarity datasets into one for each isotope, but since this difference in slopes is so small this is unnecessary. The vertical intercept value for each regression was the same across isotopes. This would indicate that the regression is robust and picking up the signal while minimizing the noise

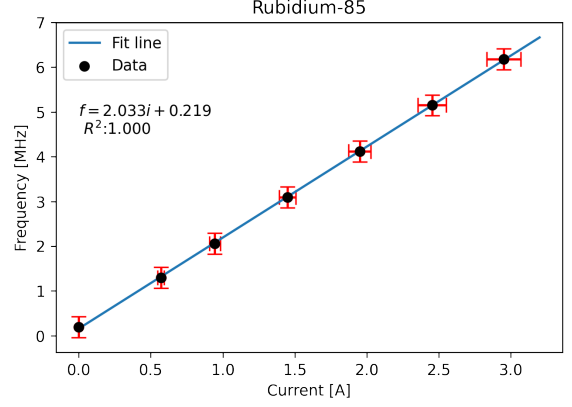


FIG. 7: Positive polarity ^{85}Rb data along with the WLS regression line.

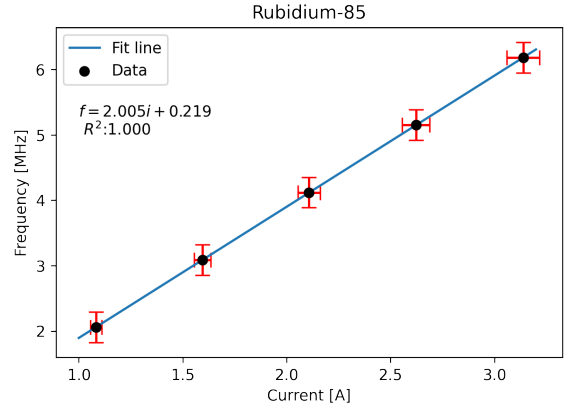


FIG. 8: Reversed polarity ^{85}Rb data along with the WLS regression line.

present within the data.

The main source of errors in determining these resonances were the difficulties in determining which lemniscate figure on the oscilloscope was the most symmetric about the horizontal and vertical axes and the ambient magnetic field within the atomic vapor cell. Trying to quantify the error due to the oscilloscope is rather difficult since there is no systematic method to determine the symmetry of the figure within the laboratory. As a result, a liberal error, σ_I , of 5% is given for each current value. From the fit, it is clear that this value is too high and should be reduced. The ambient field within the atomic cell was calculated using a prior given in [6] which quotes an average ~ 0.5 gauss at Berkeley's latitude and longitude. This error, σ_B , can be converted into a frequency error, σ_f , using the Breit-Rabi formula in equation 7. Both of these errors are represented by errorbars on the plots in Fig's 7-10.

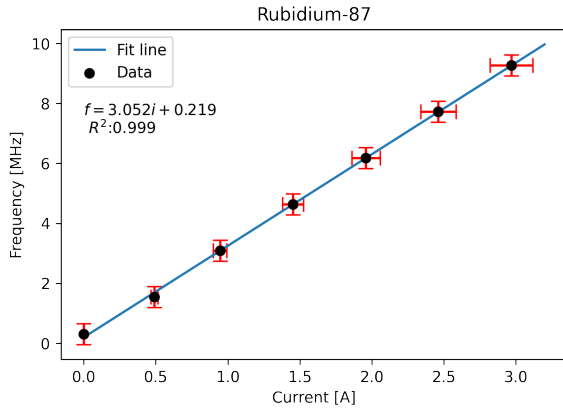


FIG. 9: Positive polarity ^{87}Rb data along with the WLS regression line.

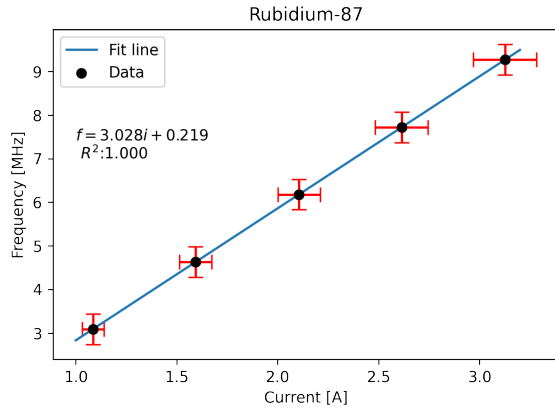


FIG. 10: Reversed polarity ^{87}Rb data along with the WLS regression line.

-
- [1] N. C. Thomas, The early history of spectroscopy, *Journal of Chemical Education* **68**, 631 (1991), <https://doi.org/10.1021/ed068p631>.
 - [2] D. J. Griffiths, *Introduction to Quantum Mechanics (2nd Edition)*, 2nd ed. (Pearson Prentice Hall, 2004).
 - [3] R. Benumof, Optical pumping theory and experiments, *American Journal of Physics* **33**, 151 (1965), <https://doi.org/10.1119/1.1971285>.
 - [4] D. Steck, Rubidium 87 d line data (2021).
 - [5] *OPT - Optical Pumping*, University of California, Berkeley.
 - [6] C. C. Finlay, S. Maus, C. D. Beggan, T. N. Bondar, A. Chambodut, T. A. Chernova, A. Chulliat, V. P. Golovkov, B. Hamilton, M. Hamoudi, R. Holme, G. Hulot, W. Kuang, B. Langlais, V. Lesur, F. J. Lowes, H. Lühr, S. MacMillan, M. Mande, S. McLean, C. Manoj, M. Menvielle, I. Michaelis, N. Olsen, J. Rauberg, M. Rother, T. J. Sabaka, A. Tangborn, L. Tøffner-Clausen, E. Thébault, A. W. P. Thomson, I. Wardinski, Z. Wei, and T. I. Zvereva, International Geomagnetic Reference Field: the eleventh generation, *Geophysical Journal International* **183**, 1216 (2010).